SCIENCE ADVANCES | RESEARCH ARTICLE

ENGINEERING

Structurally engineered ultrasoft PEDOT:PSS fiber microelectrodes with enhanced electrochemical performance for neural interfaces

Chihyeong Won[1,2]†, Young Uk Cho[3,4]†, Siyeon Kweon[5]†, Sungjoon Cho[1], Chaebeen Kwon[1], Hyun Woo Kim[1], Ju Young Lee[1], Sang Hoon Park[1], Sorim Han[5], Yang Tae Kim[6], Jumyoung Jang[6], Janghwan Jekal[8], Jae Geun Kim[6,7], Kyung-In Jang[8], Sheng Xu[9], Wei Gao[2], Il-Joo Cho[5]*, Ki Jun Yu[1,10]*, Taeyoon Lee[1]*

Stable and reliable neural interfacing is essential for the diagnosis and treatment of chronic neurological disorders. Flexible neural probes are particularly important for this purpose, as they minimize tissue damage and inflammatory responses while maintaining stable electrode-tissue coupling; however, achieving both high electrical performance and tissue-like mechanics remains challenging. Here, we present a poly(3,4-ethylenedioxythiophene) polystyrene sulfonate (PEDOT:PSS) fiber microelectrode (PFME), an all-organic neural probe capable of recording single-neuron activities with potential for long-term interfacing. The PFME is entirely composed of organic components and fabricated without thermal processing. In addition, the posttreatment process enables to selectively remove PSS binder networks while promoting PEDOT chain alignment to optimize mechanical compliance and electrochemical performance. In vivo, the PFME enables stable single-unit recordings from the mouse hippocampus. Histological analysis after 1 week of implantation reveals minimal glial activation comparable to that elicited by a conventional probe. This structurally engineered PFME establishes a pathway to achieve minimally invasive neural interfacing platforms for chronic applications.

INTRODUCTION

To understand debilitating neurological disorders such as Parkinson's disease and epilepsy, decoding the complex circuits of the brain is a central goal in neuroscience and medicine (*1*, *2*). Implantable neural interfaces provide a direct communication link between neural tissue and electronic devices and are indispensable in this endeavor. The design of these interfaces enables the recording of intricate neural signals and high-precision delivery of therapeutic electrical stimulation (*3*, *4*). Conventional neural probes, typically fabricated from rigid materials such as silicon, are extensively used for recording neural signals (*5*, *6*) but elicit chronic inflammatory responses and the formation of glial scars, owing to the mechanical mismatch between these rigid devices and soft brain tissue. The stability and quality of neural recordings are degraded by the foreign body response (FBR), as a major obstacle for long-term applications. However, developing neural interfaces that resolve these limitations while preserving the electrical performance essential for chronic applications remains a persistent challenge (*7*–*12*).

As a promising alternative for next-generation implantable neural interfaces, fiber-type electrode probes offer the inherent advantages of high structural flexibility, tailorable dimensions for scalability, and alleviated scarring of brain tissue (*13*–*15*). These flexible fibers can conform to the brain's micromotions, substantially mitigating immune responses (*16*–*18*). However, previous approaches remain constrained by intrinsic material properties and thermal-based fabrication limitations, thereby hindering electrochemical stability and structural reliability. The use of nanomaterials and polymers for replacing conventional rigid materials has also been attempted (*19*–*21*). In this regard, poly(3,4-ethylenedioxythiophene) polystyrene sulfonate (PEDOT:PSS), a conducting polymer, has earned distinction as a highly attractive material, owing to its mixed ionic-electronic conductivity, facile solution processibility, and biocompatibility (*22*–*24*). For instance, multifunctional probes capable of recording chemical and electrical signals or in vivo stimulation have been developed using support-free PEDOT:PSS fibers modified via posttreatment (*25*). As approaches for improving the electrical and electrochemical performance, PEDOT:PSS fibers have been incorporated with highly conductive materials such as MXene (*26*), carbon (*27*), or metal-based nanomaterials to form composites (*28*). Despite enhancing the electrical conductivity, these approaches often increase the mechanical rigidity of the fiber probe (in the range of hundreds of megapascals to several gigapascals), thereby exacerbating the mechanical mismatch with soft brain tissue (1 to 100 kPa) (*29*–*31*). Furthermore, although polymer-based fiber electrodes inherently have low Young's modulus suitable for soft neural interfacing, previous studies of fiber neural probes have been limited to single-channel recording due to fabrication limitations (*21*, *30*). The development of high-density, multichannel architectures of fiber neural probes without thermal process remains challenges.

---

[1] School of Electrical and Electronic Engineering, Yonsei University, Seoul 03722, Republic of Korea. [2] Andrew and Peggy Cherng Department of Medical Engineering, California Institute of Technology, Pasadena, CA 91125, USA. [3] Department of Biomedical and Robotics Engineering, Incheon National University, Incheon 22012, Republic of Korea. [4] I-Nano FAB Center, Incheon National University, Incheon 22012, Republic of Korea. [5] Department of Biomedical Sciences, College of Medicine, Korea University, Seoul 02841, Republic of Korea. [6] College of Life Sciences and Bioengineering, Incheon National University, Incheon 22012, Republic of Korea. [7] Research Center of Brain-Machine Interface, Incheon National University, Incheon 22012, Republic of Korea. [8] Department of Robotics and Mechatronics Engineering, Daegu Gyeongbuk Institute of Science and Technology (DGIST), Daegu 42988, Republic of Korea. [9] Department of Anesthesiology, Pain and Perioperative Medicine, Stanford University, Stanford, CA 94305, USA. [10] YU-Korea Institute of Science and Technology (KIST) Institute, Yonsei University, Seoul 03722, Republic of Korea.
*Corresponding author. Email: taeyoon.lee@yonsei.ac.kr (T.L.); ijcho@korea.ac.kr (I.-J.C.); kijunyu@yonsei.ac.kr (K.J.Y.)
†These authors contributed equally to this work.

In this study, the trade-off between desired properties was addressed by structurally engineering a novel PEDOT:PSS fiber microelectrode (PFME). The PFME was fabricated via wet-spinning a PEDOT:PSS colloidal gel containing sodium ions (Na^+) into an ascorbic acid (AA)–assisted coagulation bath, followed by posttreatment with phosphoric acid (H_3PO_4) and ethylene glycol (EG). The integrated process removed the structural PSS binder networks, reducing fiber rigidity while promoting realignment of PEDOT crystallites into highly conductive pathways. In contrast to thermally drawn fibers that often suffer from mechanical rigidity and limited material compatibility, the wet-spun PFMEs exhibited intrinsic softness and biocompatibility suitable for chronic neural interfacing. This fabricating approach offered reduced mechanical stiffness (0.94 N m^{-1}) and enhanced electrochemical performance, including an impedance of 0.73 kiloohm at 1 kHz and a charge storage capacity (CSC) of 59.01 mC cm^{-2}. To construct a multichannel PFME neural probe, three individual PFME fibers were assembled into a single unit via a sequential polyurethane (PU) drop-casting and encapsulation process. Integrated into a neural interface, the PFME probe enabled stable, high-fidelity neural recordings in freely moving animals over extended periods while minimizing immune responses. These findings establish PFME as a promising platform for next-generation chronic brain-machine interfaces (BMIs) for chronic disease monitoring

RESULTS

Preparation of PFME

The proposed implantable fiber neural probe is designed for a flexible BMI that combines high electrical performance with brain tissue–like mechanical properties for in vivo monitoring of chronic diseases (Fig. 1A). The probe, constructed using PFME, integrates four key attributes: (i) a simple multielectrode array configuration, (ii) a highly conductive network for efficient signal transduction, (iii) inherent elasticity to minimize mechanical mismatch with brain tissue, and (iv) biocompatibility to mitigate FBRs.

The PFME was fabricated through wet-spinning using air pressure, followed by posttreatment (Fig. 1B). The wet-spinning of PEDOT:PSS generally requires strongly dehydrating solvents [e.g., sulfuric acid (H_2SO_4) or isopropyl alcohol (IPA)] for the coagulation baths, which can cause structural deformation and compromise the mechanical integrity of the resulting fiber (*32*, *33*). To address these issues, the first step in the present strategy is the formation of a spinnable PEDOT:PSS colloidal gel via the incorporation of sodium borohydride ($NaBH_4$). During wet-spinning of PEDOT:PSS, the strong electrostatic repulsion between the negatively charged sulfonate groups of PSS chains generally causes the polymer to adopt an extended coil conformation in aqueous dispersion. This pronounced chain expansion not only lowers solution viscosity but also hampers efficient coagulation, often

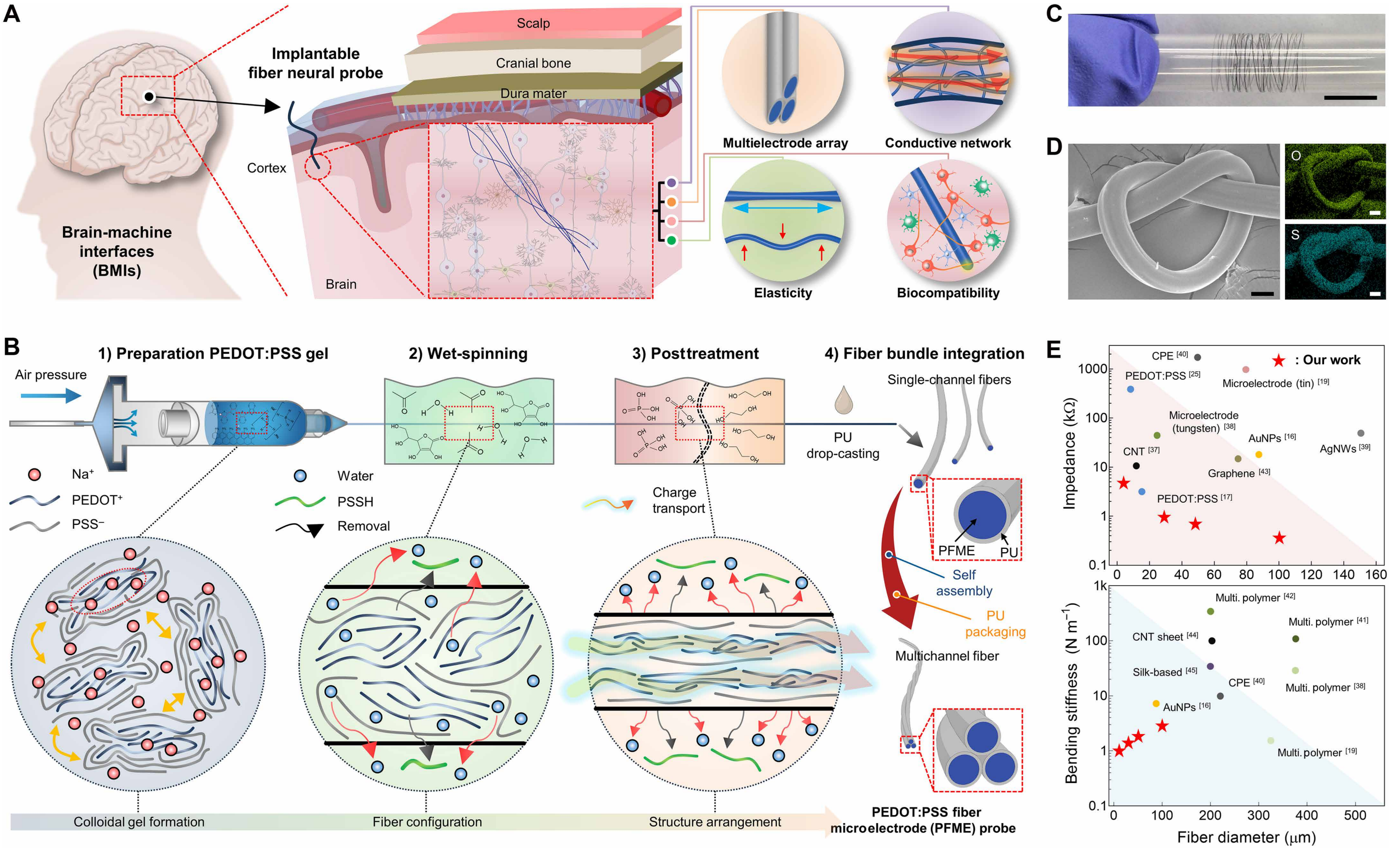

Fig. 1. Fabrication and characterization of PFMEs. (**A**) Schematic illustration of PFME as an implantable neural probe, highlighting its key properties. (**B**) Schematic illustration of modified wet-spinning process for PFME fabrication. (**C**) Optical image of a continuously collected, uniform wet-spun PFME. Scale bar, 10 mm. (**D**) Scanning electron microscope (SEM) and corresponding energy-dispersive spectroscopy (EDS) mapping images of flexible PFME. Scale bars, 30 μm. (**E**) Comparison of impedance and bending stiffness with those of other fiber-based neural probes. CPE, carbon black-doped polyethylene; AuNPs, Au nanoparticles; AgNWs, Ag nanowires; CNT, carbon nanotubes; Multi. Polymer, multifunctional polymer.

leading to discontinuous or mechanically fragile fibers. The introduction of $NaBH_4$ provides Na^+ ions that electrostatically screen these sulfonate charges, thereby mitigating the repulsive interactions among PSS backbones (*34*, *35*). This reduction in electrostatic repulsion promotes more efficient aggregation of PEDOT:PSS domains, enabling the formation of continuous, uniform fibers with improved structural integrity. In parallel, BH_4^- acts as a mild reducing agent, which can alter residual oxidative species within the PEDOT:PSS matrix and further stabilize the conductive domains (fig. S1). Collectively, these effects promote efficient aggregation of PEDOT:PSS, enabling the formation of continuous, uniform fibers with enhanced structural and electrical properties (fig. S2). However, the addition of $NaBH_4$ disrupted continuous fiber formation in conventional coagulation baths such as IPA and H_2SO_4 due to rapid dehydration and phase separation, showing nonuniform aggregation rather than continuous fibers (fig. S3). For stable fiber formation during wet-spinning, an AA-assisted acetone coagulation bath was used. The acidic AA environment kinetically retards rapid coagulation by protonating PSS chains to form polystyrene sulfonic acid (PSSH) at the fiber surface, forming a barrier that slows solvent exchange (note S1). This ensures uniform solidification throughout the fiber, minimizing internal stress. Consequently, uniform fibers were obtained, in contrast to the deformed structures produced in a pure acetone bath (fig. S4). In addition, the low-temperature process minimizes excessive PEDOT and PSS chain alignment, maintaining the intrinsic softness of the fiber. The wet-spun fibers were then posttreated with H_3PO_4 and EG to simultaneously optimize electrical and mechanical properties. Multichannel packaging of PFMEs was easily achieved by PU coating and its interfacial adhesion. The PFME was coated with a uniform, thin layer of PU using a drop-casting method for insulating except to a cross-sectional recording site (fig. S5). A self-assembly behavior between the PU coatings allowed the fibers to aggregate into a compact configuration that minimizes surface area, effectively forming a tightly integrated bundle without complex packaging techniques. The diameter of each PFME can be readily tuned by varying the nozzle size during the wet-spinning process (fig. S6).

This optimized process enables the high-throughput production of long and uniform PFMEs (Fig. 1C). The morphology and composition of the fibers were characterized by scanning electron microscopy (SEM) and energy-dispersive spectroscopy (EDS) (Fig. 1D). SEM image revealed a twisted, seamless surface morphology indicative of high flexibility, while corresponding EDS mapping of O and S confirmed the homogeneous distribution of PEDOT:PSS throughout the fiber. Molecular-level changes induced by posttreatment were analyzed using Raman spectroscopy to validate the effect of the posttreatment processes (fig. S7). First, protonation of the PSS sulfonate groups through H_3PO_4 treatment weakens the coulombic association between $PEDOT^+$ and PSS^-, driving phase redistribution in which excess, electrically insulating PSS is expelled during the subsequent rinse. The resulting PEDOT-rich network exhibits increased domain connectivity and reduced electronic path tortuosity. Concomitantly, the acidic environment induces electrostatic screening and dehydration promoting conformational planarization of the PEDOT chains and tighter π-π stacking, which together enhance carrier mobility. These bulk reorganizations decrease the fiber's series resistance. This mechanism is demonstrated in x-ray photoelectron spectroscopy (XPS) analysis, with decreased PSS chains (fig. S8). Second, EG treatment induces a conformational change in PEDOT chains from a coiled benzoid to a more linear quinoid structure, favorable for charge transport (*36*). Shifts in the characteristic vibrational peaks of the Fourier transform infrared spectra confirm these structural changes in the PEDOT:PSS network following EG treatment (fig. S9). Notably, combined H_3PO_4 and EG treatment promotes a transformation to the quinoid form, suggesting a synergistic effect in which PSS removal facilitates subsequent PEDOT core rearrangement. These complementary mechanisms directly demonstrate that the posttreatment strategy effectively modifies the conductive network of PFME, yielding superior electrical performance. Compared with state-of-the-art fiber-based neural probes, the PFME simultaneously offers optimized electrical and mechanical properties (Fig. 1E and table S1) (*16*, *17*, *19*, *25*, *37*–*45*). The structurally engineered PFME combines ultralow impedance with tissue-like bending stiffness, outperforming existing probes. Its impedance is markedly lower than that of conducting polymer or carbon-based fiber electrodes of similar diameter. Furthermore, its bending stiffness is orders of magnitude lower than that of multifunctional polymers and carbon nanotube fibers and comparable to soft hydrogels, which are typically constrained by poor electrical properties. In addition, the PFME exhibits electrochemical charge storage and charge injection capacities that are sufficient for stable neural recording and stimulation as a fiber neural probe. This synergistic optimization positions PFME as a promising neural probe for minimally invasive brain interfaces and long-term neural modulation.

Mechanism underlying concurrently optimized properties and characterization of PFME

The electrical and mechanical properties of PFME were improved through the distinct roles of each processing step (Fig. 2A and note S2). First, the AA-assisted acetone coagulation bath controlled the formation of the initial PEDOT:PSS fiber. Unlike pure acetone, which induces rapid coagulation and deformed structures, AA-assisted acetone modulates coagulation kinetics. Protonation and partial removal of PSS chains as PSSH at the fiber surface generated a temporary barrier that slowed solvent exchange, ensuring uniform solidification and minimizing internal stress (*46*, *47*). Second, sequential posttreatment with H_3PO_4 and EG synergistically enhanced both electrical and mechanical properties. The first step, H_3PO_4 treatment, selectively removes the structural PSS network that acts as a rigid binder in the gelled fiber. Its removal establishes direct connections between PEDOT molecules, eliminates insulating barriers, and induces structural relaxation, thereby improving mechanical properties (*48*, *49*). In the subsequent step, EG penetrates the newly formed porous structure and optimizes fiber properties. Acting as a plasticizer, EG enhances flexibility and stretchability while also inducing a conformational change in PEDOT chains from the coiled, low-conductivity benzoid state to the linear, high-conductivity quinoid structure, thus creating efficient charge transport pathways (*50*).

The enhanced electrochemical properties were evaluated in vitro by measuring the electrochemical impedance of PFMEs with various diameters, tailored by changing the nozzle diameter during the wet-spinning process. The PFME surface was coated with a conformal PU encapsulation layer. The recording site was exposed by partially cross-sectioning the PFME while the surrounding regions remained insulation. The impedance of each fiber was measured using electrochemical impedance spectroscopy (EIS) in the frequency range of 10^{-3} to 10^2 kHz (Fig. 2B). As shown in the electrochemical impedance spectra, the impedance decreased as the diameter of the fiber increased, attributed to the large electrode-electrolyte interfacial

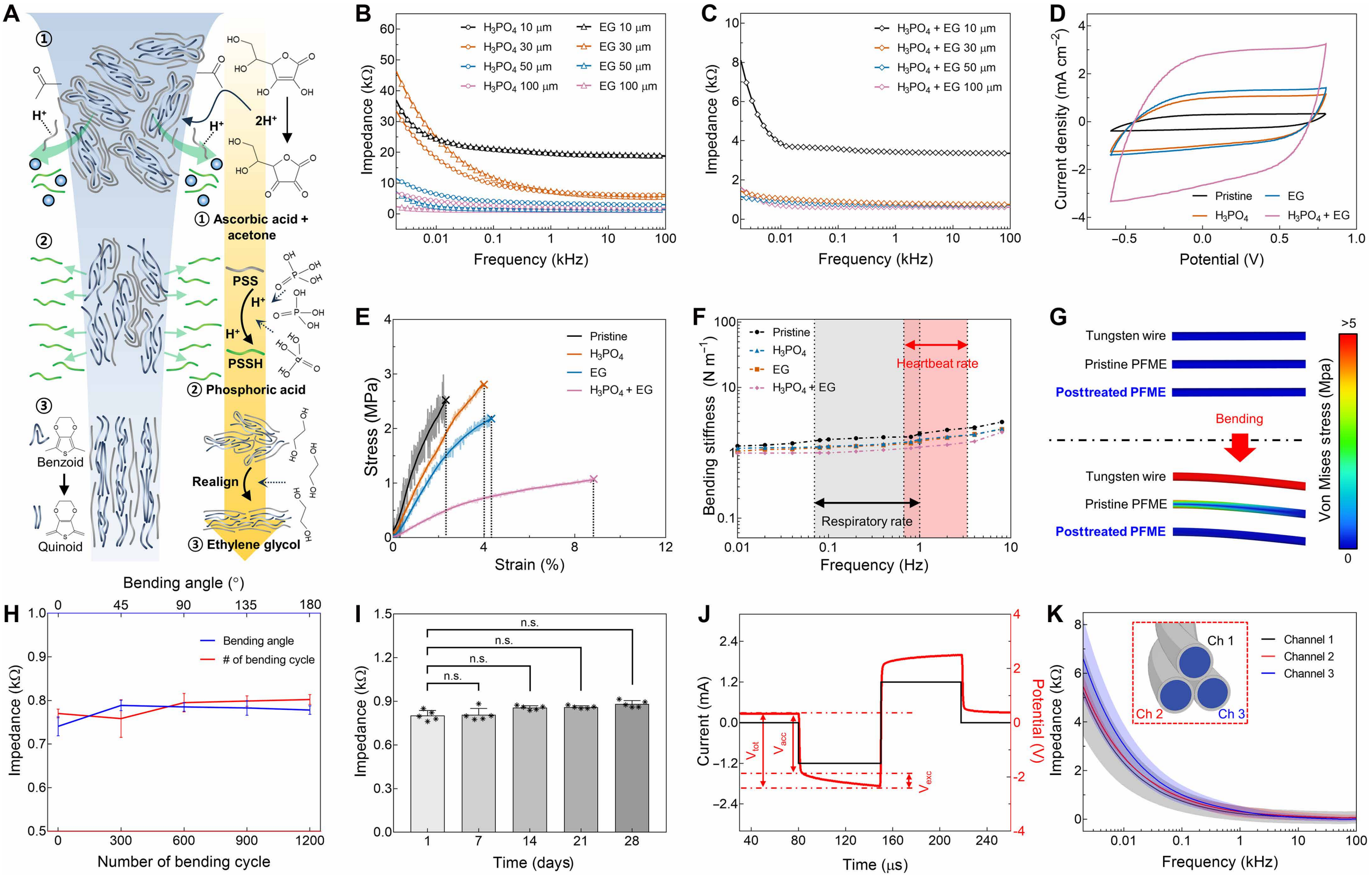

Fig. 2. Electrical, electrochemical, and mechanical properties of PFMEs. (**A**) Schematic diagram of the PFME coagulation and posttreatment steps. (**B** and **C**) Impedance spectra of PFMEs with various diameters, modified with different posttreatment solutions; H_3PO_4 and EG individually (B) and a combination of both (C). (**D** and **E**) Cyclic voltammetry (CV) (D) and strain-stress (E) curves of the PFMEs modified with different posttreatment solutions. (**F**) Bending stiffness of PFMEs measured over frequency range of 0.01 to 10 Hz ($n = 5$). (**G**) Von Mises stress distribution in stainless steel, pristine PFME, and posttreated PFME probe under bending deformation. (**H**) Impedance spectra of PFME probe measured at different bending angles and over repetitive bending cycles. (**I**) Impedance stability of PFME probe over 28 days in a brain phantom of 1% agarose. One-way analysis of variance (ANOVA) and Dunnett's multiple-comparison test: $P = 0.9830$, $P = 0.7330$, $P = 0.7421$, and $P = 0.7191$. Values in (H) and (I) represent the mean and the SD ($n = 5$). n.s., not significant. (**J**) Voltage transient response of PFME to a 1.2-mA biphasic current pulse. (**K**) Impedance of three-channel PFME probe across separate channels.

area. For the fibers treated with H_3PO_4, increasing the diameter from 10 to 100 μm caused the impedance at 1 kHz to decrease from 19.49 to 2.08 kiloohm, and a similar trend (19.87 to 1.36 kiloohm) was observed for the EG-treated fibers. Despite single treatments, the impedance of small-diameter fibers remained relatively high. In contrast, combined H_3PO_4 and EG treatment produced a clear synergistic effect, yielding substantially lower impedance across all diameters (3.42, 0.80, 0.73, and 0.62 kiloohm for 10-, 30-, 50-, and 100-μm fibers, respectively) (Fig. 2C). This corresponds to an area-normalized impedance of 0.0027 ohm cm^2, approximately 67 times lower than that of previously reported PEDOT:PSS electrodes (*35*). Cyclic voltammetry (CV) analysis of the pristine (untreated), H_3PO_4-treated, EG-treated, and combined H_3PO_4 and EG-treated fibers provided further evidence of the enhanced electrochemical performance (Fig. 2D). The CSC, an indicator of the amount of charge available for transfer at the electrode-electrolyte interface, was calculated from the enclosed area of the CV curve and normalized to the geometric cross-sectional area of the PFME recording site (fig. S10). The CSC was substantially larger for PFME subjected to the combined treatment than for the pristine fibers and those subjected to the single treatments. Specifically, the calculated CSC of the fiber modified by combined treatment was 59.02 mC cm^{-2}, representing an approximately 8.4 times increase relative to that of the pristine fiber (7.01 mC cm^{-2}). This enhanced CSC is crucial for neural recording, as it contributes to lowering the noise level and improving the signal-to-noise ratio (SNR).

The mechanical properties of the posttreated PFME were evaluated under tensile strain (Fig. 2E). The stress-strain curves of the pristine PFME are characterized by a rapid increase in stress with strain, corresponding to a relatively high Young's modulus of 746.3 kPa and a low fracture strain of 2.31%. In contrast, the Young's modulus of the PFMEs treated with either H_3PO_4 or EG treatment was reduced, and the fracture strain increased. Notably, the greatest improvement was achieved with combined H_3PO_4 and EG treatment, yielding the lowest Young's modulus (50.4 kPa) and highest fracture strain (8.7%). Enhanced flexibility was further confirmed by bending stiffness measurements (Fig. 2F and fig. S11). Bending stiffness decreased from 2.07 N m^{-1} for the pristine fiber to 1.22 N m^{-1} after combined treatment and remained stable across the frequency range relevant to physiological brain micromotions, respiration, and heartbeat. Finite element analysis (FEA) simulations compared stress distributions in a tungsten wire, pristine PFME, and posttreated PFME under bending deformation (Fig. 2G). For samples with identical dimensions (100-μm diameter and 1000-μm length), the posttreated PFME exhibited substantially lower and more uniform stress distribution than both the tungsten wire and pristine PFME, consistent with bending stiffness results.

The electrical stability of the PFME probe under mechanical stress and simulated long-term implantation was evaluated to assess its suitability for chronic applications. Impedance remained stable within 5% across bending angles from 0° to 180° and after 1200 bending cycles (Fig. 2H and fig. S12). Continuous in vitro impedance monitoring in a brain phantom (1% agarose) showed less than 3% variation from the initial value after 28 days, underscoring the probe's stability for long-term recording (Fig. 2I). In addition, the PFME maintained its stability under hydrated conditions (fig. S13). In addition, the low impedance and high CSC of the PFME demonstrated that a PFME probe has potential to be suitable for safe and effective electrical stimulation for neural modulation (Fig. 2J). The minimal negative potential excursion (V_{exc}), which is the difference between the total voltage (V_{tot}) and the access voltage (V_{acc}), confirms the PFME's high charge injection capacity and ability to deliver stimulation currents up to 1.2 mA safely, corresponding to a charge injection capacity of 11.88 mC cm^{-2}. Impedance measurements from three distinct channels (Ch 1, Ch 2, and Ch 3) in a PFME bundle probe demonstrated clear separation without electrical cross-talk (Fig. 2K and fig. S14). The consistent and independent impedance profiles across all channels confirm the reliability of the multichannel configuration and the integrity of each electrode within the bundled probe.

Analysis of PFME formation and microstructural compositions

The formation of stable, uniform fibers is an essential step for fabricating high-performance PFMEs for neural probes. The coagulation behavior of the Na$^+$-induced PEDOT:PSS colloidal gel was therefore evaluated. When extruded into deionized (DI) water, the gel rapidly dispersed and failed to form continuous filaments. In contrast, extrusion into the optimized AA-assisted acetone coagulation bath produced stable, self-supporting fibers (Fig. 3A). The stability of these filaments is attributed to the cohesive Na$^+$-induced gel network, which is critical for effective solidification during wet-spinning.

Although Na$^+$-induced gelation imparts the structural integrity required for spinning, the coagulation bath composition dictates PFME morphology and uniformity (*51*). Fiber morphology is critically influenced by dehydration dynamics in each type of coagulation bath (Fig. 3B). Dehydration of PEDOT:PSS gels generates substantial internal stress from capillary forces, which can induce structural deformation (*52*). In DI water (a), fibers readily disperse because of the absence of a coagulant. In the case of an acetone (b), rapid surface dehydration produces a steep stress gradient between the solidified skin and wet core. Once dynamic networks form within the gel, this nonuniform stress drives disordered polymer chain reorganization, resulting in macroscopic deformation. In the optimized AA-assisted acetone bath (c), coagulation kinetics are modulated to enable gradual uniform solidification from surface to core, promoting ordered polymer network alignment (fig. S15). Consequently, fiber deformation can be precisely controlled by adjusting the AA concentration.

On the basis of mechanisms of gelation and coagulation kinetics, fabrication parameters were systematically optimized to establish ideal conditions for producing uniform, high-quality fibers. Spinning outcomes were mapped as a function of NaBH$_4$ concentration in the PEDOT:PSS structures and AA concentration in the coagulation bath, yielding a spinnability phase diagram (Fig. 3C). The map defines three regimes: a nonspinnable region, typically at low NaBH$_4$ concentrations where the gel lacks cohesion; a deformable region, where fibers with structural defects form; and an optimal spinnable region (*53*). The nonspinnable boundaries arise from two distinct failure mechanisms: insufficient ionic cross-linking at low NaBH$_4$ concentrations prevents filament formation, while excessive cross-linking at high concentrations produces a brittle gel prone to fracture during extrusion. Likewise, high AA concentrations increase the water requirement for dissolution, reducing the dehydrating capacity of the acetone bath and hindering effective coagulation. Overall, the phase diagram identifies a processing window within which continuously spinnable, uniform fibers can be reliably produced. The electrical and mechanical reliability of the fibers fabricated within the deformable and optimized spinnable regions was confirmed through repetitive bending tests (Fig. 3D). After 10,000 bending cycles, the relative change in electrical resistance [$\Delta R/R_0$ (%), $\Delta R = R - R_0$] of the deformed increased by ~9.33%, whereas the bending stiffness decreased by 61.7%. This substantial degradation is attributed to the nonuniform internal structure of the fibers, which renders the conductive network susceptible to failure and compromises the mechanical resilience. In contrast, the uniform fiber demonstrated superior stability, with a negligible change in the electrical resistance ($\Delta R/R_0$ of 0.27%) decrease in the bending stiffness by only 16.5%, demonstrating the superior resilience of these fibers to mechanical deformation.

To define the microstructural origins of these enhanced properties, we performed FEA to investigate the internal stress distribution within the fiber during formation (Fig. 3E). As the concentration of AA increased, the von Mises stress distribution within the fiber under deformation became substantially more uniform. These results align with the dehydration model of the developed fiber, in which modified coagulation kinetics generate a more homogeneous stress profile. Overall, the AA-assisted coagulation bath minimizes internal stress concentrations, producing a mechanically robust and homogeneous fiber structure. In addition, the molecular alignment within the internal structures of the uniform and deformed fibers was comparatively analyzed using two-dimensional (2D) small-angle x-ray scattering (SAXS) (*32*). The SAXS profile of the deformed fiber was characterized by a relatively isotropic scattering pattern with broad, ringlike features, indicating randomly oriented polymer chains (Fig. 3F). In contrast, the uniform fiber exhibited highly anisotropic, arc-like scattering patterns concentrated along the meridional direction, indicative of strong preferential alignment of polymer chains along the fiber axis (Fig. 3G). Quantitative analysis of 1D scattering profiles integrated along the equatorial (q_y) direction (Fig. 3H) revealed sharper, more intense diffraction peaks corresponding to lamellar stacking of PEDOT and PSS domains and π-π stacking of PEDOT chains. The increased intensity and reduced peak width indicate higher crystallinity and larger crystalline domains in the uniform fiber. This highly ordered, aligned microstructure, enabled by the optimized fabrication process, underpins both the soft mechanical properties and the efficient charge transport pathways. It is the fundamental origin of the concurrently optimized properties of PFME, enabling its function as an effective neural probe.

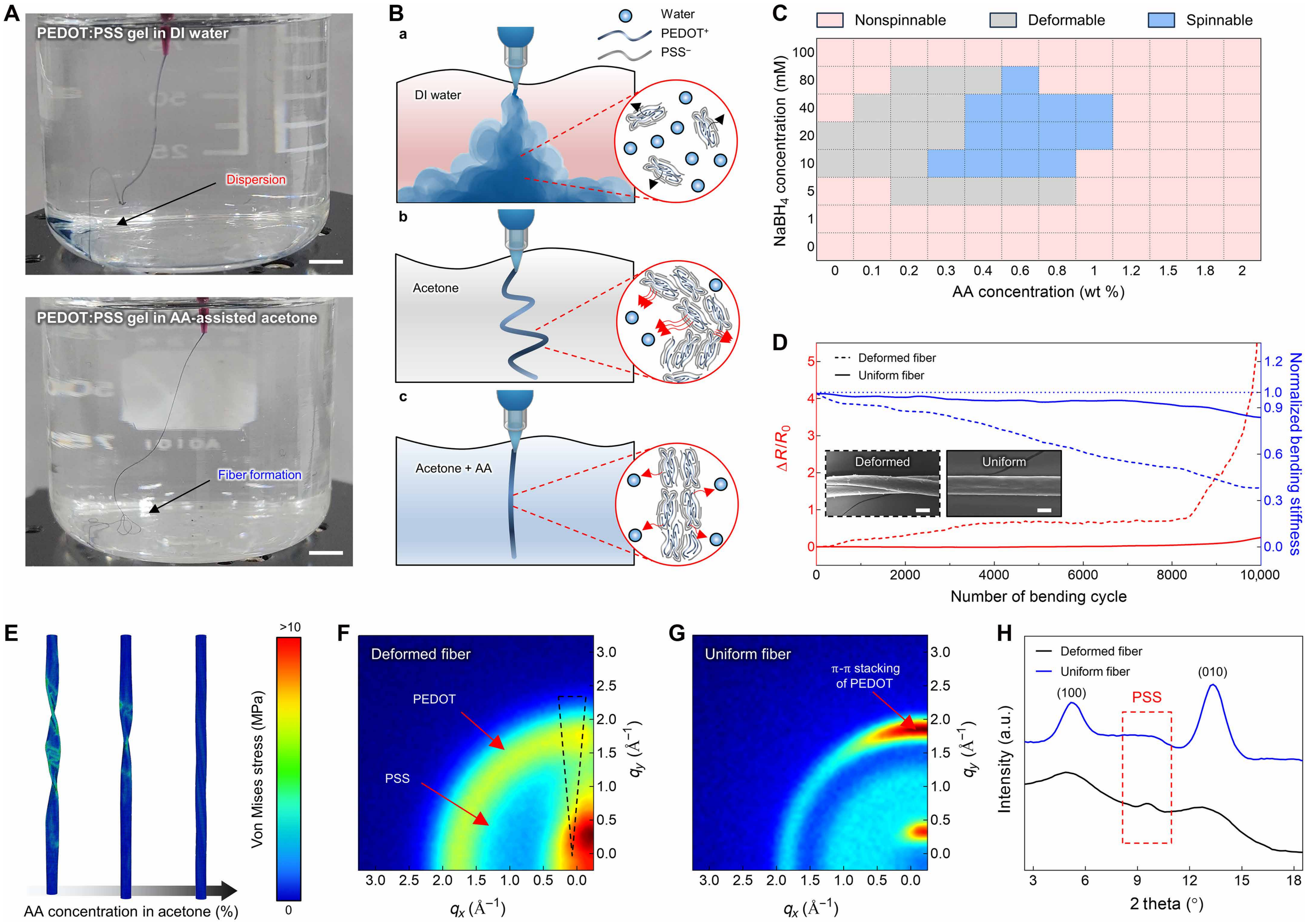

Fig. 3. Mechanism of structural engineering and microstructural compositions of PFMEs. (**A**) Optical images of a PEDOT:PSS gel extruded into (top) DI water and (bottom) coagulation solution. Scale bars, 10 mm. (**B**) Schematic illustration of morphological changes in wet-spun PFMEs depending on coagulation solutions. (**C**) Suitable concentration profiles of AA in coagulation solution and NaBH4 in PEDOT:PSS gel for wet-spinning. (**D**) Electrical and mechanical durability of probes using deformed and uniform PFME under repetitive bending test over 10,000 cycles. The insets show top-view SEM images of deformed and uniform fibers. Scale bars, 10 μm. (**E**) FEA simulation of stress distribution in PFMEs fabricated in acetone coagulation solutions with varying AA concentrations. (**F** and **G**) Small-angle x-ray scattering (SAXS) patterns of the deformed (F) and uniform (G) PFMEs. (**H**) Corresponding SAXS profile of the deformed and uniform PFMEs along the q_y direction, as indicated by the dashed line in (F). a.u., arbitrary units.

In vivo performance and biocompatibility of PFME as a neural probe

A custom-printed circuit board brain chip was integrated with a three-channel neural probe by twisting and packaging three individual PFMEs. The assembly was implanted into a mouse brain to validate in vivo functionality (Fig. 4A and fig. S16). The implanted probe features uncoated PEDOT:PSS electrodes for connection to the brain chip, fiber tips as recording sites, and a PU–polyethylene glycol (PEG) encapsulation layer. The dual-layer encapsulation follows a previously reported method (*16*): PU serves as the electrical insulator, while PEG acts as a dissolvable shuttle, temporarily increasing stiffness to facilitate implantation. The PEG layer began dissolving within seconds of exposure to physiological brain fluids and was completely degraded within ~3 min (fig. S17). Cross-sectional SEM image of the tightly bundled three-channel structure shows well-separated recording sites conformally coated with a thin (~3 μm) PU layer, and corresponding EDS mapping confirmed the elemental composition of the recording sites (Fig. 4B).

The enhanced electrical and mechanical properties of the PFME probe enabled highly reliable in vivo neural recordings. Spontaneous activity from the hippocampus region (anteroposterior (AP) = −1.8, mediolateral (ML) = 1.6, dorsoventral (DV) = 1.5 mm) was continuously recorded, and spike signals were sorted across all three channels (Fig. 4C). High-amplitude spikes were distinguishable from noise and background activity, enabling the identification of multiple, distinct single-neuron units per channel. For example, spike sorting from channel 2 identified two distinct units with SNRs of 16.46 (peak amplitude: −68.09 μV) and 19.45 (peak amplitude: −83.53 μV), respectively. Four distinct single-neuron units were identified across all channels, each with characteristic waveforms and firing rates of 1.26 to 4.33 Hz (Fig. 4D). To further validate spike-sorting quality, we analyzed the extracted waveforms by principal components

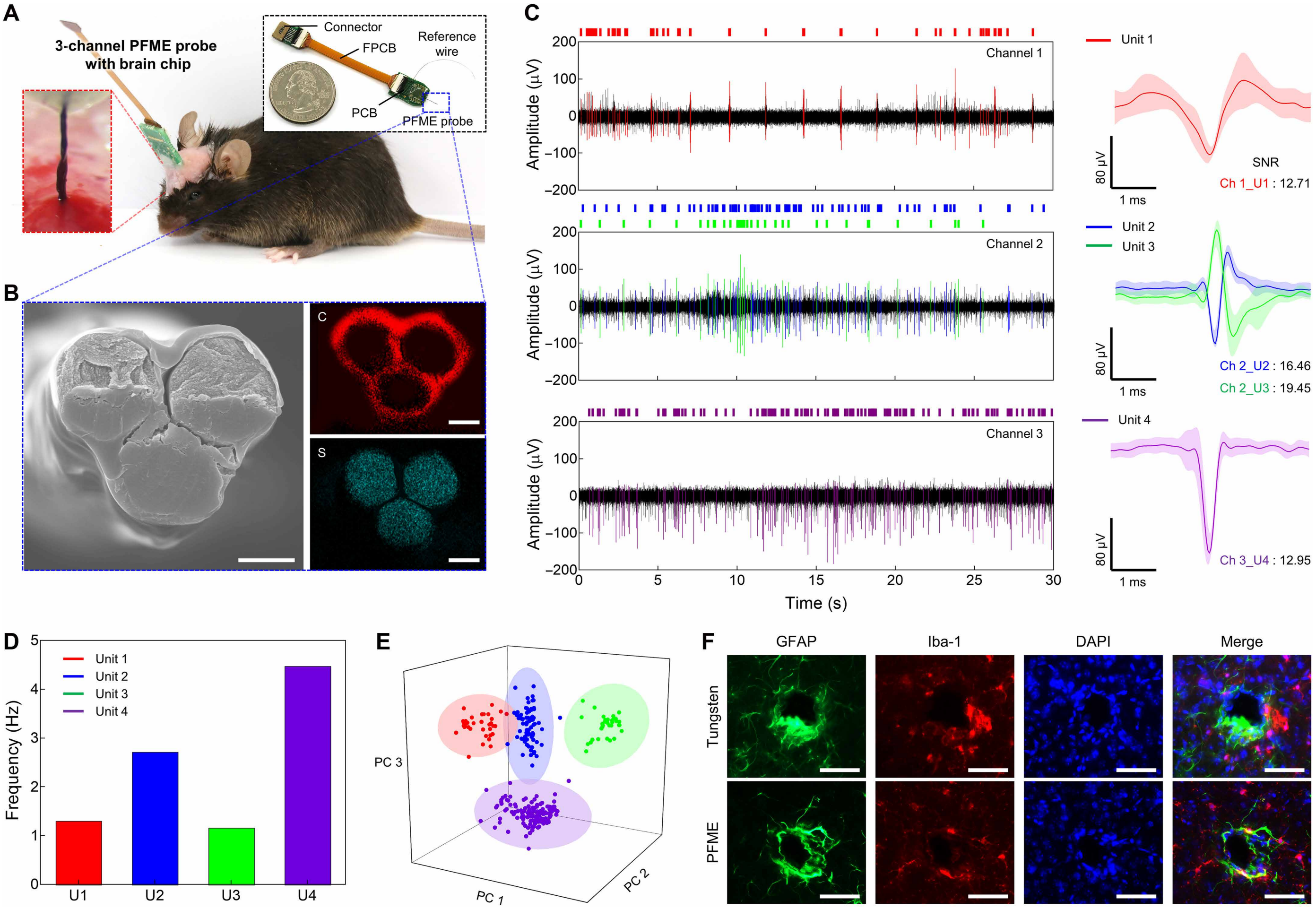

Fig. 4. Mechanism of structural engineering and microstructural compositions of PFMEs. (**A**) Optical image of three-channel PFME probe with a brain chip implanted in a mouse. The black inlet shows the overall device layout, and the red inset exhibits the three-channel PFME probe implanted in the brain. (**B**) The SEM and EDS mapping images of recording sites of the probe, and the blue inlet in (A). Scale bars, 30 μm. (**C**) Recorded raw neural spike signals and corresponding sorted spike units from the hippocampus region through each channel of PFME probe. (**D**) Firing rate of five individual units. (**E**) 3D principal components analysis (PCA) results with distinct clusters of neuron units. (**F**) Immunofluorescence analysis of glial activation around two types of implanted fiber probes (tungsten wire and PFME) at 1 week postimplantation. Scale bars, 50 μm.

analysis (PCA). The 3D PCA plot revealed four segregated clusters in feature space, confirming that signals from each neuron were sufficiently distinct for reliable separation (Fig. 4E). This high neuronal yield from a minimally invasive probe underscores its efficiency in monitoring local microcircuit activity without larger, more damaging implants. The ability to resolve multiple neurons per channel further demonstrates the probe's high spatial resolution and sensitivity. To access the long-term stability of the PFME, we performed an accelerated soaking test in phosphate-buffered saline (PBS) at 67°C (fig. S18). The impedance of the PFME showed negligible variation for 7 days, demonstrating electrochemical stability and indicating potential for chronic neural recording applications.

To evaluate the biocompatibility of the developed PFME probe, we assessed neuroglial activation that serves as a pathological marker for inflammation and neuronal injury. Histological analyses were performed at 1-week postimplantation of both a tungsten wire and the PFME by detecting immunosignals of glial fibrillary acidic protein (GFAP) and ionized calcium-binding adapter molecule 1 (Iba-1), molecular markers of astrocytes and microglia, respectively (Fig. 4F and fig. S19). Immunofluorescence imaging revealed a dense accumulation of GFAP-positive astrocytes and Iba-1–positive microglia surrounding the implantation site in both groups, with comparable spatial distribution and overlap in the merged images. Quantitative fluorescence intensity profiles along the implantation tract further confirmed that the peak signals of GFAP and Iba-1 were comparable between tungsten wire– and PFME-implanted brains, indicating no substantial difference in the extent of astrocytic and microglial activation (fig. S20). The comparable level of glial activation suggests the translational potential of the PFME as a soft neural interface with biocompatibility comparable to that of conventional neural probes.

DISCUSSION

In summary, an implantable PFME probe was reported to overcome the trade-off between mechanical softness and electrical performance for neural interfaces. Using a fully organic, low-temperature fabrication route combining PEDOT:PSS colloidal gelation, coagulation-modulated bath, and posttreatment, the PFME was developed to have ultrasoft mechanical characteristics and high conductivity. This process selectively removes the structural PSS binder, substantially reducing mechanical stiffness while realigning PEDOT crystallites, thereby enhancing the electrical and electrochemical properties of the fiber. Integrated with a brain chip, the PFME enabled in vivo recording of hippocampal neural signals in brain of mice. As a three-channel neural probe, it reliably isolated high-resolution single-neuron spikes from multiple channels. The tissue-like mechanical stiffness of the PFME led to comparable glial scarring and immune responses to those observed with conventional probes. Overall, PFME fabrication via structural engineering provides a versatile platform for next-generation minimally invasive, biocompatible, and chronically stable brain interfaces for both fundamental neuroscience and potential clinical applications.

MATERIALS AND METHODS

Materials

A 1.3 wt % aqueous PEDOT:PSS solution (Clevios PH-1000) was purchased from Heraeus. PU granule (Estane 58887; nominal size: 3 to 5 mm) was obtained from Goodfellow, UK. Acetone (99.5%), H_3PO_4 (85 wt % in H_2O), EG (99.5%), and IPA (99.5%) were purchased from Duksan Integrated Science, Korea. Sodium borohydride (powder) was obtained from Daejung Chemicals & Metals, Korea. L-AA (99%), PEG (M_w average: 4000), tetrahydrofuran (99%), *N*,*N*-dimethylformamide (99%), 2,2,2-tribromoethanol (97%), Triton X-100, and anti-GFAP antibody (1:1000; G6171) were purchased from Sigma-Aldrich, Germany. Rabbit anti–Iba-1 antibody (1:1000; 019-19741) was purchased from FUJIFILM Wako, Japan. Goat anti-rabbit Alexa Fluor 594 (1:1000; A11037, Invitrogen) and goat anti-mouse Alexa Fluor 488 secondary antibody (1:1000; A11001, Invitrogen) were obtained from Thermo Fisher Scientific, USA. Fluoroshield Mounting Medium containing 4′,6-diamidino-2-phenylindole (DAPI; ab104139) was purchased from Abcam, UK. Nozzles (tip size: 18 to 32 gauge) for wet-spinning were obtained from Nordson EFD, USA.

Fabrication of the PFME

The PEDOT:PSS colloidal gel was prepared by mixing a 0.01 M $NaBH_4$ into PEDOT:PSS solution (Clevios PH-1000), followed by baking for 48 hours at 50°C to remove moisture and stirring for 12 hours to homogenize the mixture. The gel was poured into a 10-ml syringe (Optimum syringe barrels, Nordson EFD), which was then connected to a custom-made air pump system equipped with an air regulator (KPR201-02BT-4, KCC, Korea) that can adjust the air pressure in the range of 0.35 to 1.5 psi. The optimized coagulation bath consisted of acetone and 2 wt % L-AA in DI water in a 7:3 volume ratio. The fibers were formed by wet-spinning PEDOT:PSS in the developed coagulation bath, followed by immersion in H_3PO_4 and EG for 30 min, respectively, to enhance the electrical and mechanical performance of the PFME. After cleaning the PFME using IPA, the fibers were encapsulated with 5 wt % PU in tetrahydrofuran and *N*,*N*-dimethylformamide [75/25 (v/v) %] solvent. The diameter of the PFME was controlled by changing the nozzle tip (32-, 27-, 25-, 20-, and 18-gauge needle for 5, 10, 30, 50, and 100 μm of PFME, respectively).

Packaging of the PFME probe

A three-channel PFME probe was packaged in PU using the same method used for coating the single fibers. The probe was then coated with PEG as a biodegradable shuttle to confer temporary rigidity, enabling implantation in the brain. After coating, one end of the probe was cut with a surgical blade (Ailee Co. Ltd., Korea) to reveal the recording site. The other side was connected to the brain chip using silver paste. A reference wire was used with the probe, and all exposed parts were coated with thermal paste (EPO-TEK 320, Epoxy Technology Inc., USA). The device was connected to an Omnetics connector (Minneapolis, USA) through a customized flexible printed circuit board (FPCB), which allowed integration with the Intan board for recording neural signals.

Structural and chemical characterization of the PFME

Raman spectra (LabRAM Aramis, Horiba Jobin Yvon, Japan) were acquired using a 514-nm excitation laser by scanning the Raman shift in the range of 900 to 1730 cm^{-1}. All fiber samples were placed on a glass substrate and fixed at both ends with polyimide tape. XPS measurement was carried out with K_α XPS [XPS(mono)] (K-Alpha, Thermo Fisher Scientific. UK). All samples were prepared with the solid-type fibers and evaluated using depth profiling analysis. In situ high-resolution x-ray diffraction (SmartLab, Rigaku, Japan) analysis with 2D time-resolved SAXS/wide-angle x-ray scattering (2D TR-SAXS/WAXS) was conducted using a 9-kW x-ray power generator. The data were integrated within a ±5° range along the meridional and equatorial directions using X-ray Microdiffraction Analysis Software to characterize the anisotropic scattering. The surface morphology of the PFME was characterized using a field-emission SEM (FE-SEM; 7610FPlus, JEOL). Cross-sectional SEM imaging and corresponding EDS mapping of the PFME were further performed using the same FE-SEM integrated with an EDS system. The particle size distribution and zeta potential were analyzed using a Particle Size and Zeta Potential Analyzer (ELS-Z1000, Otsuka Electronics). Ultraviolet-visible (UV-Vis)–near infrared absorption spectra were recorded using a UV/VIS spectrophotometer (V-650, JASCO).

Electrical/electrochemical and mechanical characterization of the PFME

Electrical measurements were performed using a digital source meter (B2901A, Keysight Technologies) and an EIS system (VersaSTAT 3, AMETEK, Princeton Applied Research). CV of PFME was conducted at a scan rate of 50 mV s^{-1}. Impedance spectra were recorded from 10^{-3} to 10^2 kHz, with the PFME recording region serving as the working electrode and a reference electrode immersed in PBS. Mechanical properties were assessed using a custom 1D stretching system and a bending setup with one end of the fiber fixed, coupled to a force transducer (S2M, HBM); 4-mm-long fiber samples were mounted on the testing stage. To evaluate the long-term electrochemical stability of the PFME, an accelerated soaking test was conducted on the basis of the Arrhenius time-temperature relationship. The equivalence between accelerated and physiological conditions was estimated using a Q_{10} model, expressed as $Q_{10} = \left(R_2/R_1\right)^{10/(T_2-T_1)}$, where R_1 and R_2 are the reaction rates at temperature T_1 and T_2, respectively. Q_{10} represents the temperature coefficient (typically 2 to 3), so 7 days at 67°C corresponds to ~2 to 6 months at 37°C.

FEA simulation of PFME

FEA simulations were performed using Abaqus/CAE. 3D fiber models (30-μm diameter and 1000-μm length) were constructed to evaluate bending stiffness, parameterized by elastic modulus, Poisson's ratio, and density. Fiber deformation induced by the coagulation bath was simulated using thermal shrinkage as the driving mechanism. A vertical force (F) was applied at the midpoint between the two fixed ends, and the resulting displacement (u) and bending stiffness (K) were calculated as $K = Fu^{-1}$. Theoretical stiffness was estimated using $K_{\text{theory}} = (3\pi E d^4)\,(64L^3)^{-1}$, where E is the elastic modulus, d is the diameter, and L is the fiber length. An electrostatic behavior was modeled using a heat transfer analogy for simulating the spatial distribution of electrical potential and access interchannel electrical isolation. Simulation results showed good agreement with the analytical solution.

In vivo recording of neural signals using PFME probe

All animal procedures were approved by the Institutional Animal Care and Use Committee (IACUC) of Korea University College of Medicine (approval no. KOREA-2023-0088) and were conducted in accordance with institutional guidelines. The PFME probe was implanted in an adult male wild-type mouse (C57BL/6; 8 weeks, 30 g). Anesthesia was induced with 3.0% isoflurane in O_2/N_2O and maintained at 1.0% isoflurane. The mouse was fixed in a stereotaxic apparatus (David Kopf Instruments, USA), the scalp was incised, and the skull and dura over the recording site were carefully removed according to Paxinos and Franklin's atlas. Spontaneous neural activity was recorded from the hippocampus (AP = −1.8, ML = −1.6, DV = +1.5 mm relative to Bregma), with a reference wire placed on the contralateral cortex. Neural signals were acquired using an Intan recording system (RHD2000 Evaluation System, Intan Technologies, USA) and processed with the Intan software (sampling rate: 20 kS s^{-1} per channel; 60-Hz notch filter; band-pass filtering: 0.1 to 6 kHz for local field potentials and 300 to 6000 Hz for single-unit spikes).

Surgical procedure and tissue preparation

Electrodes were stereotaxically implanted at an anteroposterior coordinate relative to Bregma (ML = −1.0 mm) and lowered to a depth of 2.0 mm from the cortical surface. The implants were secured with dental cement. One week after implantation of tungsten wires or PFMEs, mice were deeply anesthetized with tribromoethanol. They were then perfused with 0.9% saline, followed by 4% paraformaldehyde (PFA) in PBS. Brains were carefully extracted and postfixed in 4% PFA for 24 hours at 4°C before further processing.

Immunohistochemistry

Horizontal brain sections (50 μm of thickness) were prepared using a vibratome (5100 mz, Campden Instruments Ltd., Leicestershire, UK). Sections were preincubated with 0.3% Triton X-100 in phosphate buffer (PB) for 30 min at room temperature (RT). After several washes with PB, sections were incubated overnight at 4°C with anti–Iba-1 antibody and anti-GFAP antibody. The following day, sections were washed with PB for 30 min and incubated at RT with Alexa Fluor 594 and Alexa Fluor 488 secondary antibody. Last, sections were mounted on glass slides with DAPI mounting medium, covered with coverslips, and sealed with nail polish to prevent drying. Fluorescence microscopy (Axioplan 2 Imaging, Carl Zeiss Microimaging Inc., Oberkochen, Germany) was used to capture images of Iba-1– and GFAP-positive cells. The Iba-1– and GFAP-positive signals were quantified using ImageJ by an independent observer to ensure unbiased counts. In addition to cell quantification, line profile analysis was performed in ImageJ by drawing a straight region of interest across the probe-tissue interface, and the fluorescence intensity was plotted as a function of distance from the interface. Background-subtracted values were expressed in arbitrary units and compared between groups.

Supplementary Materials

This PDF file includes:
Notes S1 and S2
Figs. S1 to S20
Table S1

REFERENCES

1. K. Asanuma, C. Tang, Y. Ma, V. Dhawan, P. Mattis, C. Edwards, M. G. Kaplitt, A. Feigin, D. Eidelberg, Network modulation in the treatment of Parkinson's disease. *Brain* **129**, 2667–2678 (2006).
2. P. Ryvlin, S. Rheims, L. J. Hirsch, A. Sokolov, L. Jehi, Neuromodulation in epilepsy: State-of-the-art approved therapies. *Lancet Neurol.* **20**, 1038–1047 (2021).
3. M. Zhang, Z. Tang, X. Liu, J. Van der Spiegel, Electronic neural interfaces. *Nat. Electron.* **3**, 191–200 (2020).
4. T. D. Y. Kozai, N. B. Langhals, P. R. Patel, X. Deng, H. Zhang, K. L. Smith, J. Lahann, N. A. Kotov, D. R. Kipke, Ultrasmall implantable composite microelectrodes with bioactive surfaces for chronic neural interfaces. *Nat. Mater.* **11**, 1065–1073 (2012).
5. J. J. Jun, N. A. Steinmetz, J. H. Siegle, D. J. Denman, M. Bauza, B. Barbarits, A. K. Lee, C. A. Anastassiou, A. Andrei, Ç. Aydın, M. Barbic, T. J. Blanche, V. Bonin, J. Couto, B. Dutta, S. L. Gratiy, D. A. Gutnisky, M. Häusser, B. Karsh, P. Ledochowitsch, C. M. Lopez, C. Mitelut, S. Musa, M. Okun, M. Pachitariu, J. Putzeys, P. D. Rich, C. Rossant, W. Sun, K. Svoboda, M. Carandini, K. D. Harris, C. Koch, J. O'Keefe, T. D. Harris, Fully integrated silicon probes for high-density recording of neural activity. *Nature* **551**, 232–236 (2017).
6. U. Chae, J. Woo, Y. Cho, J.-K. Han, S. H. Yang, E. Yang, H. Shin, H. Kim, H.-Y. Yu, C. J. Lee, I.-J. Cho, A neural probe for concurrent real-time measurement of multiple neurochemicals with electrophysiology in multiple brain regions in vivo. *Proc. Natl. Acad. Sci. U.S.A.* **120**, e2219231120 (2023).
7. J. J. Clark, S. G. Sandberg, M. J. Wanat, J. O. Gan, E. A. Horne, A. S. Hart, C. A. Akers, J. G. Parker, I. Willuhn, V. Martinez, S. B. Evans, N. Stella, P. E. M. Phillips, Chronic microsensors for longitudinal, subsecond dopamine detection in behaving animals. *Nat. Methods* **7**, 126–129 (2010).
8. Y. Guo, S. Jiang, B. J. B. Grena, I. F. Kimbrough, E. G. Thompson, Y. Fink, H. Sontheimer, T. Yoshinobu, X. Jia, Polymer composite with carbon nanofibers aligned during thermal drawing as a microelectrode for chronic neural interfaces. *ACS Nano* **11**, 6574–6585 (2017).
9. L. Gao, J. Wang, Y. Zhao, H. Li, M. Liu, J. Ding, H. Tian, S. Guan, Y. Fang, Free-standing nanofilm electrode arrays for long-term stable neural interfacings. *Adv. Mater.* **34**, e2107343 (2022).
10. Y. Lee, H. Shin, D. Lee, S. Choi, I.-J. Cho, J. Seo, A lubricated nonimmunogenic neural probe for acute insertion trauma minimization and long-term signal recording. *Adv. Sci.* **8**, e2100231 (2021).
11. T. M. Fu, G. Hong, T. Zhou, T. G. Schuhmann, R. D. Viveros, C. M. Lieber, Stable long-term chronic brain mapping at the single-neuron level. *Nat. Methods* **13**, 875–882 (2016).
12. C. Won, C. Kwon, K. Park, J. Seo, T. Lee, Electronic drugs: Spatial and temporal medical treatment of human diseases. *Adv. Mater.* **33**, e2005930 (2021).
13. S. Park, G. Loke, Y. Fink, P. Anikeeva, Flexible fiber-based optoelectronics for neural interfaces. *Chem. Soc. Rev.* **48**, 1826–1852 (2019).
14. C. Won, S. Cho, K.-I. Jang, J.-U. Park, J. H. Cho, T. Lee, Emerging fiber-based neural interfaces with conductive composites. *Mater. Horiz.* **12**, 4545–4572 (2025).
15. Y. Zhang, J. Ding, B. Qi, W. Tao, J. Wang, C. Zhao, H. Peng, J. Shi, Multifunctional fibers to shape future biomedical devices. *Adv. Funct. Mater.* **29**, 1902834 (2019).
16. C. Won, U.-J. Jeong, S. Lee, M. Lee, C. Kwon, S. Cho, K. Yoon, S. Lee, D. Chun, I.-J. Cho, T. Lee, Mechanically tissue-like and highly conductive Au nanoparticles embedded elastomeric fiber electrodes of brain–machine interfaces for chronic in vivo brain neural recording. *Adv. Funct. Mater.* **32**, 2205145 (2022).
17. C. Tang, Z. Han, Z. Liu, W. Li, J. Shen, K. Zhang, S. Mai, J. Li, X. Sun, X. Chen, H. Li, L. Wang, J. Liang, M. Liao, J. Feng, C. Wang, J. Wang, L. Ye, Y. Yang, S. Xie, X. Shi, K. Zeng, X. Zhang, X. Cheng, K. Zhang, Y. Guo, H. Yang, Y. Xu, Q. Tong, H. Yu, P. Chen, H. Peng, X. Sun, A soft-fiber bioelectronic device with axon-like architecture enables reliable neural recording in vivo under vigorous activities. *Adv. Mater.* **36**, e2407874 (2024).
18. Y. Kim, Y. Lee, J. Yoo, K. S. Nam, W. Jeon, S. Lee, S. Park, Multifunctional and flexible neural probe with thermally drawn fibers for bidirectional synaptic probing in the brain. *ACS Nano* **18**, 13277–13285 (2024).
19. S. Park, H. Yuk, R. Zhao, Y. S. Yim, E. W. Woldeghebriel, J. Kang, A. Canales, Y. Fink, G. B. Choi, X. Zhao, P. Anikeeva, Adaptive and multifunctional hydrogel hybrid probes for long-term sensing and modulation of neural activity. *Nat. Commun.* **12**, 3435 (2021).

20. J. Feng, C. Chen, X. Sun, H. Peng, Implantable fiber biosensors based on carbon nanotubes. *Acc. Mater. Res.* **2**, 138–146 (2021).
21. L. Bi, R. Garg, N. Noriega, R. J. Wang, H. Kim, K. Vorotilo, J. C. Burrell, C. E. Shuck, F. Vitale, B. A. Patel, Y. Gogotsi, Soft, multifunctional MXene-coated fiber microelectrodes for biointerfacing. *ACS Nano* **18**, 23217–23231 (2024).
22. J. Rivnay, S. Inal, B. A. Collins, M. Sessolo, E. Stavrinidou, X. Strakosas, C. Tassone, D. M. Delongchamp, G. G. Malliaras, Structural control of mixed ionic and electronic transport in conducting polymers. *Nat. Commun.* **7**, 11287 (2016).
23. G. Huseynova, Y. H. Kim, J.-H. Lee, J. Lee, Rising advancements in the application of PEDOT:PSS as a prosperous transparent and flexible electrode material for solution-processed organic electronics. *J. Inf. Disp.* **21**, 71–91 (2020).
24. T. Yang, M. Yang, C. Xu, K. Yang, Y. Su, Y. Ye, L. Dou, Q. Yang, W. Ke, B. Wang, Z. Luo, PEDOT:PSS hydrogels with high conductivity and biocompatibility for in situ cell sensing. *J. Mater. Chem. B* **11**, 3226–3235 (2023).
25. T. Xu, W. Ji, X. Wang, Y. Zhang, H. Zeng, L. Mao, M. Zhang, Support-free PEDOT:PSS fibers as multifunctional microelectrodes for in vivo neural recording and modulation. *Angew. Chem. Int. Ed.* **61**, e202115074 (2022).
26. S. Gou, P. Li, S. Yang, G. Bi, Z. Du, High-performance MXene/PEDOT-PSS microscale fiber electrodes for neural recording and stimulation. *Adv. Funct. Mater.* **35**, 2424236 (2025).
27. C. Xu, S. Yang, P. Li, H. Wang, H. Li, Z. Liu, Wet-spun PEDOT:PSS/CNT composite fibers for wearable thermoelectric energy harvesting. *Compos. Commun.* **32**, 101179 (2022).
28. P. GhavamiNejad, A. GhavamiNejad, H. Zheng, K. Dhingra, M. Samarikhalaj, M. Poudineh, A conductive hydrogel microneedle-based assay integrating PEDOT:PSS and Ag-Pt nanoparticles for real-time, enzyme-less, and electrochemical sensing of glucose. *Adv. Healthc. Mater.* **12**, e2202362 (2023).
29. J. R. Capadona, D. J. Tyler, C. A. Zorman, S. J. Rowan, C. Weder, Mechanically adaptive nanocomposites for neural interfacing. *MRS Bull.* **37**, 581–589 (2012).
30. C. Tang, S. Xie, M. Wang, J. Feng, Z. Han, X. Wu, L. Wang, C. Chen, J. Wang, L. Jiang, P. Chen, X. Sun, H. Peng, A fiber-shaped neural probe with alterable elastic moduli for direct implantation and stable electronic–brain interfaces. *J. Mater. Chem. B* **8**, 4387–4394 (2020).
31. Y. Ziai, S. S. Zargarian, C. Rinoldi, P. Nakielski, A. Sola, M. Lanzi, Y. B. Truong, F. Pierini, Conducting polymer-based nanostructured materials for brain–machine interfaces. *Wiley Interdiscip. Rev. Nanomed. Nanobiotechnol.* **15**, e1895 (2023).
32. J. Zhang, S. Seyedin, S. Qin, P. A. Lynch, Z. Wang, W. Yang, X. Wang, J. M. Razal, Fast and scalable wet-spinning of highly conductive PEDOT:PSS fibers enables versatile applications. *J. Mater. Chem. A* **7**, 6401–6410 (2019).
33. H. Chen, H. Xu, M. Luo, W. Wang, X. Qing, Y. Lu, Q. Liu, L. Yang, W. Zhong, M. Li, D. Wang, Highly conductive, ultrastrong, and flexible wet-spun PEDOT:PSS/ionic liquid fibers for wearable electronics. *ACS Appl. Mater. Interfaces* **15**, 20346–20357 (2023).
34. Q. Li, Q. Zhou, L. Wen, W. Liu, Enhanced thermoelectric performances of flexible PEDOT:PSS film by synergistically tuning the ordering structure and oxidation state. *J. Mater.* **6**, 119–127 (2020).
35. H. W. Kim, J. Kim, J. Y. Kim, K. Kim, J. Y. Lee, T. Kim, S. Cho, J. Bin An, H. J. Kim, L. Sun, S. Lee, K. Fukuda, T. Someya, M. Sang, Y. U. Cho, J. E. Lee, K. J. Yu, Transparent, metal-free PEDOT:PSS neural interfaces for simultaneous recording of low-noise electrophysiology and artifact-free two-photon imaging. *Nat. Commun.* **16**, 4032 (2025).
36. Y.-Y. Deng, X.-L. Shi, T. Wu, Y. Yue, W.-D. Liu, M. Li, F. Yue, P. Huang, Q. Liu, Z.-G. Chen, Optimization of wet-spun PEDOT:PSS fibers for thermoelectric applications through innovative triple post-treatments. *Adv. Fiber Mater.* **6**, 1616–1628 (2024).
37. F. Vitale, S. R. Summerson, B. Aazhang, C. Kemere, M. Pasquali, Neural stimulation and recording with bidirectional, soft carbon nanotube fiber microelectrodes. *ACS Nano* **9**, 4465–4474 (2015).
38. A. Sahasrabudhe, L. E. Rupprecht, S. Orguc, T. Khudiyev, T. Tanaka, J. Sands, W. Zhu, A. Tabet, M. Manthey, H. Allen, G. Loke, M.-J. Antonini, D. Rosenfeld, J. Park, I. C. Garwood, W. Yan, F. Niroui, Y. Fink, A. Chandrakasan, D. V. Bohórquez, P. Anikeeva, Multifunctional microelectronic fibers enable wireless modulation of gut and brain neural circuits. *Nat. Biotechnol.* **42**, 892–904 (2024).
39. C. Lu, S. Park, T. J. Richner, A. Derry, I. Brown, C. Hou, S. Rao, J. Kang, C. T. Moritz, Y. Fink, P. Anikeeva, Flexible and stretchable nanowire-coated fibers for optoelectronic probing of spinal cord circuits. *Sci. Adv.* **3**, e1600955 (2017).
40. C. Lu, U. P. Froriep, R. A. Koppes, A. Canales, V. Caggiano, J. Selvidge, E. Bizzi, P. Anikeeva, Polymer fiber probes enable optical control of spinal cord and muscle function in vivo. *Adv. Funct. Mater.* **24**, 6594–6600 (2014).
41. A. Canales, X. Jia, U. P. Froriep, R. A. Koppes, C. M. Tringides, J. Selvidge, C. Lu, C. Hou, L. Wei, Y. Fink, P. Anikeeva, Multifunctional fibers for simultaneous optical, electrical and chemical interrogation of neural circuits in vivo. *Nat. Biotechnol.* **33**, 277–284 (2015).
42. M. Du, L. Huang, J. Zheng, Y. Xi, Y. Dai, W. Zhang, W. Yan, G. Tao, J. Qiu, K.-F. So, C. Ren, S. Zhou, Flexible fiber probe for efficient neural stimulation and detection. *Adv. Sci.* **7**, 2001410 (2020).
43. S. Zhao, G. Li, C. Tong, W. Chen, P. Wang, J. Dai, X. Fu, Z. Xu, X. Liu, L. Lu, Z. Liang, X. Duan, Full activation pattern mapping by simultaneous deep brain stimulation and fMRI with graphene fiber electrodes. *Nat. Commun.* **11**, 1788 (2020).
44. W. Jeon, J. M. Lee, Y. Kim, Y. Lee, J. Won, S. Lee, W. Son, Y. H. Koo, J.-W. Hong, H. Gwac, J. Joo, S. J. Kim, C. Choi, S. Park, Structurally aligned multifunctional neural probe using forest-drawn CNT sheet onto thermally drawn polymer fiber for long-term in vivo operation. *Adv. Mater.* **36**, e2313625 (2024).
45. Y. Zhou, C. Gu, J. Liang, B. Zhang, H. Yang, Z. Zhou, M. Li, L. Sun, T. H. Tao, X. Wei, A silk-based self-adaptive flexible opto-electro neural probe. *Microsyst. Nanoeng.* **8**, 118 (2022).
46. J. Liu, G. Liu, J. Xu, C. Liu, W. Zhou, P. Liu, G. Nie, X. Duan, F. Jiang, Graphene/polymer hybrid fiber with enhanced fracture elongation for thermoelectric energy harvesting. *ACS Appl. Energy Mater.* **3**, 6165–6171 (2020).
47. J. H. Song, J. Park, S. H. Kim, J. Kwak, Vitamin C-induced enhanced performance of PEDOT:PSS thin films for eco-friendly transient thermoelectrics. *ACS Appl. Mater. Interfaces* **15**, 2852–2860 (2023).
48. B. J. Worfolk, S. C. Andrews, S. Park, J. Reinspach, N. Liu, M. F. Toney, S. C. B. Mannsfeld, Z. Bao, Ultrahigh electrical conductivity in solution-sheared polymeric transparent films. *Proc. Natl. Acad. Sci. U.S.A.* **112**, 14138–14143 (2015).
49. Z. Fan, P. Li, D. Du, J. Ouyang, Significantly enhanced thermoelectric properties of PEDOT:PSS films through sequential post-treatments with common acids and bases. *Adv. Energy Mater.* **7**, 1602116 (2017).
50. H. Okuzaki, Y. Harashina, H. Yan, Highly conductive PEDOT/PSS microfibers fabricated by wet-spinning and dip-treatment in ethylene glycol. *Eur. Polym. J.* **45**, 256–261 (2009).
51. D. Lyu, Y. Jin, P. C. M. M. Magusin, S. Sturniolo, E. W. Zhao, S. Yamamoto, S. T. Keene, G. G. Malliaras, C. P. Grey, Operando NMR electrochemical gating studies of ion dynamics in PEDOT:PSS. *Nat. Mater.* **22**, 746–753 (2023).
52. D. Xu, X. Meng, S. Liu, J. Poisson, P. Vana, K. Zhang, Dehydration regulates structural reorganization of dynamic hydrogels. *Nat. Commun.* **15**, 6886 (2024).
53. X. Xie, Z. Xu, X. Yu, H. Jiang, H. Li, W. Feng, Liquid-in-liquid printing of 3D and mechanically tunable conductive hydrogels. *Nat. Commun.* **14**, 4289 (2023).

Acknowledgments: We thank Yonsei Graduate School for support through the International Joint Research Grant. We also acknowledge technical support from the I-Nano FAB at Incheon National University. **Funding:** This work was supported by the National Research Foundation of Korea (NRF) grant funded by the Korea government (MSIT) (nos. RS-2023-00234581, RS-2024-00336147, and RS-2024-00460364) (T.L.). This work was supported by the Technology Innovation Program (RS-2025-02304448; Development of a patient-tailored, cervical-worn wearable electronic drug based on multiple external stimulation therapy for dysphagia rehabilitation) funded by the Ministry of Trade, Industry & Energy (MOTIE, Korea) (T.L.). This work was supported by the National Research Foundation of Korea (NRF) grant funded by the Korea government (MSIT) (RS-2024-00353768, RS-2025-02217919, RS-2025-02215070, and RS-2025-18362970) (K.J.Y.). This study was funded by the Yonsei Fellowship funded by Lee Youn Jae and the KIST Institutional Program Project (No. 26E0161-26-050) (K.J.Y.). This work was also supported by the Global Education and Research Center for Convergence Technology through the Brain Korea 21 Four Program, Yonsei University (T.L. and K.J.Y.). This research was supported by the Basic Science Research Program through the National Research Foundation of Korea (NRF) funded by the Ministry of Education (RS-2025-02413549) (C.W.). This work was supported by the National Research Foundation of Korea (NRF) grant funded by the Korea government (MSIT) (RS-2025-23323516) (Y.U.C.). **Author contributions:** Conceptualization: C.W., T.L., Y.U.C., K.-I.J., and K.J.Y. Methodology: C.W., S.K., H.W.K., S.H.P., J.G.K., K.-I.J., K.J.Y., T.L., and S.H. Investigation: C.W., Y.U.C., S.K., S.C., C.K., S.H.P., S.H., Y.T.K., J.Ja., K.-I.J., I.-J.C., and K.J.Y. Visualization: C.W., Y.U.C., C.K., Y.T.K., J.Ja., K.-I.J., K.J.Y., and T.L. Supervision: T.L., K.-I.J., W.G., I.-J.C., and K.J.Y. Writing—original draft: C.W., Y.U.C., K.-I.J., I.-J.C., K.J.Y., and T.L. Writing—review and editing: C.W., Y.U.C., S.K., S.H., J.Je., S.X., K.-I.J., W.G., I.-J.C., K.J.Y., and T.L. Resources: T.L., C.W., Y.U.C., J.G.K., K.-I.J., I.-J.C., and K.J.Y. Funding acquisition: T.L., C.W., K.-I.J., and K.J.Y. Data curation: C.W., Y.U.C., S.K., S.C., S.H., J.G.K., K.-I.J., I.-J.C., and K.J.Y. Validation: C.W., Y.U.C., H.W.K., J.Y.L., Y.T.K., J.Ja., K.-I.J., I.-J.C., and K.J.Y. Formal analysis: C.W., Y.U.C., S.K., H.W.K., S.H., K.-I.J., I.-J.C., and K.J.Y. Software: C.W., S.H.P., K.-I.J., and K.J.Y. Project administration: T.L., C.W., K.-I.J., and K.J.Y. **Competing interests:** The authors declare that they have no competing interests. **Data, code, and materials availability:** All data and code needed to evaluate and reproduce the results in the paper are present in the paper and/or the Supplementary Materials. No new materials have been created for this work.

Submitted 26 November 2025
Accepted 17 April 2026
Published 27 May 2026
10.1126/sciadv.aee2754

Science Advances

Structurally engineered ultrasoft PEDOT:PSS fiber microelectrodes with enhanced electrochemical performance for neural interfaces

Chihyeong Won, Young Uk Cho, Siyeon Kweon, Sungjoon Cho, Chaebeen Kwon, Hyun Woo Kim, Ju Young Lee, Sang Hoon Park, Sorim Han, Yang Tae Kim, Jumyoung Jang, Janghwan Jekal, Jae Geun Kim, Kyung-In Jang, Sheng Xu, Wei Gao, Il-Joo Cho, Ki Jun Yu, and Taeyoon Lee

Sci. Adv. **12** (22), eaee2754. DOI: 10.1126/sciadv.aee2754

Science Advances (ISSN 2375-2548) is published by the American Association for the Advancement of Science. 1200 New York Avenue NW, Washington, DC 20005. The title *Science Advances* is a registered trademark of AAAS.